

# Internal magnetic field structures observed by PSP/WISPR in a filament related coronal mass ejection

G.M. Cappello<sup>1</sup>, M. Temmer<sup>1</sup>, A. Vourlidas<sup>2</sup>, C. Braga<sup>2</sup>, P.C. Liewer<sup>3</sup>, J. Qiu<sup>4</sup>,  
G. Stenborg<sup>2</sup>, A. Kouloumvakos<sup>2</sup>, A.M. Veronig<sup>1,5</sup>, V. Bothmer<sup>6</sup>

<sup>1</sup> Institute of Physics, University of Graz, Universitätsplatz 5, 8010 Graz, Austria  
e-mail: greta.cappello@uni-graz.at

<sup>2</sup> The Johns Hopkins University Applied Physics Laboratory, 11101 Johns Hopkins Road, Laurel, MD 20723, USA.

<sup>3</sup> Jet Propulsion Laboratory, California Institute of Technology, Pasadena, CA, 91109, USA

<sup>4</sup> Department of Physics, Montana State University, Bozeman, MT, 59717, USA

<sup>5</sup> Kanzelhöhe Observatory for Solar and Environmental Research, University of Graz, 9521 Treffen, Austria

<sup>6</sup> Institut für Astrophysik und Geophysik, Georg-August-Universität, Göttingen, Germany

Received February 14, 2024; accepted

## ABSTRACT

**Context.** We track and investigate from white-light data taken with the Wide-field Instrument for Solar PRobe (WISPR) aboard Parker Solar Probe (PSP), localized density enhancements, reflecting small-scale magnetic structures belonging to a filament-related coronal mass ejection (CME).

**Aims.** We aim to investigate the 3D location, morphology and evolution of the internal magnetic fine structures of CMEs. Specifically, we ask: what is the physical origin of the small-scales in the WISPR images? How do these structures evolve over time? What is their relationship with the filament/source region and the flux rope?

**Methods.** The fast tangential motion of the PSP spacecraft during its perihelion permits viewing the same event from multiple angles in short times relative to the event's evolution. Hence, we can derive the three-dimensional information of selected CME features from a single spacecraft using triangulation techniques.

**Results.** We group small-scale structures with roughly similar speeds, longitude and latitude, into three distinct morphological groups. We find twisted magnetic field patterns close to the eastern leg of the CME that may be related to 'horns' outlining the edges of the flux-rope cavity. Aligned thread-like bundles are identified close to the western leg. They may be related to confined density enhancements evolving during the filament eruption. High density blob-like features (magnetic islands) are widely spread in longitude ( $\sim 40^\circ$ ) close to the flanks and rear part of the CME. We also note that the large-scale outer envelope of the CME, seen clearly from 1 AU, is not well observed in PSP.

**Conclusions.** We demonstrate that CME flux ropes may comprise different morphological groups with a cluster behavior, apart from the blobs which instead span a wide range of longitudes. This may hint either to the three-dimensionality of the post-CME current sheet (CS) or to the influence of the ambient corona in the evolutionary behavior of the CS. Importantly, we show that the global appearance of the CME can be very different in WISPR (0.11–0.16 AU) and instruments near 1 AU because of shorter line-of-sight integration of WISPR.

**Key words.** coronal mass ejections – triangulation – 3D reconstruction – small scale features – internal structures – parker solar probe

## 1. Introduction

Coronal mass ejections (CMEs) refer to the substantial expulsion of plasma and magnetic flux from the solar corona into interplanetary space. Their driver is a magnetic flux rope structure, which may not necessarily contain cold filamentary material (e.g., Chen 2011), accelerated outward by magnetic reconnection through the Lorentz force (Forbes 2000; Vršnak 2001). Using multiple viewpoints of CMEs through stereoscopic coronagraph images from the Solar TERrestrial RELations Observatory (STEREO, Kaiser et al. 2008), we have gained valuable insights about their three-dimensionality when observed from 1 AU. Typically, but not always, we observe a CME morphology that includes a faint front (a shock sheath if the CME is fast enough) followed by a bright loop-like leading edge, and then a dim region corresponding to a low plasma-beta structure delineating the flux rope (Vourlidas et al. 2013; Temmer & Both-

mer 2022). When interacting with the near-Earth environment, CMEs can drive a variety of space weather effects, such as geomagnetic storms, disruption of satellite communication systems or ground-induced currents (see reviews by e.g., Pulkkinen 2007; Gopalswamy 2022). Hence, the evolution of CMEs from Sun to Earth has received particular attention over the years. Several recent reviews give an overview of our current understanding of the physics of CME evolution, their interaction with the ambient solar wind, state-of-the-art modeling and analysis methods, and the gaps that we need to fill in the future (e.g., Green et al. 2018; Temmer 2021; Zhang et al. 2021; Gopalswamy 2022; Mishra & Teriaca 2023; Temmer et al. 2023).

There are clear associations of CMEs with phenomena observed on the solar disk, such as flares, filament/prominence eruptions, coronal waves, or dimming regions, etc. (see e.g., Chen 2011). Note that in this manuscript we will use the terms 'filament' and 'prominence' interchangeably, since we study ob-

servations from different viewpoints and both terms refer to the same physical phenomenon. Specifically, filaments are considered as proxies of sheared magnetic field arcades (DeVore & Antiochos 2000), and magnetic flux ropes (MFRs), snaking along and above the neutral line (e.g., Moore et al. 2001; Amari et al. 2003). Statistical studies find that more than 80% of erupting filaments are associated with a CME (e.g., Schmieder et al. 2013). They are particularly well observed in chromospheric spectral lines, like  $H\alpha$ , and cool EUV lines, e.g., HeI 304Å (e.g., Parenti 2014; Chen et al. 2014).

High-resolution observations indicate that filaments are composed of a collection of thin threads situated above the photospheric magnetic neutral line (e.g., Tandberg-Hanssen 1995; Aulanier & Schmieder 2002; Okamoto et al. 2007). Horizontal threads may be associated with cool material suspended between the dips of a sheared arcade or twisted flux rope, while vertical threads are not yet well understood (see e.g., Su et al. 2015; Guo et al. 2021). Schmieder et al. (2014) and Ruan et al. (2018) argued that vertical threads are due to the accumulation of many small dips containing short threads.

Although small-scale CME structures have been studied in the past, the accessible scales depend on the resolution of the imaging instrument at hand. Every new generation of white-light instruments reveals ever finer details about the internal structures of CMEs and their evolution (Howard et al. 2023). Here, we investigate a variety of transient density enhancements to trace the magnetic fine structure of a filament-related CME observed by the Wide-Field Imager for Solar PRobe (WISPR; Vourlidis et al. 2016) onboard the Parker Solar Probe (PSP; Fox et al. 2016).

WISPR provides stunning views of the off-limb corona with higher sensitivity compared to coronagraphic imagery from missions located near 1 AU, such as the Solar and Heliospheric Observatory (SOHO, see Brueckner et al. 1995), Domingo et al. (1995) and STEREO (see Kaiser et al. 2008; Howard et al. 2008). Illing & Hundhausen (1983) first identified looplike structures, visible within the ejecta, as bright coronal material in the form of a concave upward arch in images from the Solar Maximum Mission (SMM; Bohlin et al. 1980). These fine structures, namely the ‘horns’, were also observed by Vourlidis et al. (2013) in SOHO coronagraphic images. They highlight the magnetic flux rope (MFR) nature of the cavity. Webb & Cliver (1995) and Webb et al. (2003) performed statistical studies on SMM data on concave-outward regions, finding that about half of them were followed by coaxial and bright rays, suggesting the formation of the current sheets. The latter, usually depicted as a 2D surface, may last several hours and extends in the outer corona. Post-CME blobs are usually related to the post-CME current sheet and plasmoid instabilities such as magnetic islands (see, e.g., Ciaravella & Raymond 2008; Schanche et al. 2016; Webb & Vourlidis 2016; Lee et al. 2020). Many simulations were performed to understand the nature of these blobs. For example, Riley et al. (2007) considered bursty reconnection in the current sheet, as modeled by a MHD simulation, and suggested the formation of blobs and their acceleration along the rays through the energy released during the reconnection process. Also, Poirier et al. (2023) modeled blobs by simulating an intermittent release of density structures generated by tearing-induced magnetic reconnection at the tip of helmet streamers and propagating in the slow solar wind.

WISPR has already made close-up views of CMEs, e.g., for distances of  $\sim 0.062$  AU during Encounter 10 (E10). (Howard et al. 2022) highlighted the presence of brightness inhomogeneities that appear as blobs and smaller MFR structures within the larger MFR. Patel et al. (2023) studied an arc-shaped

concave-up structure in a WISPR CME. In addition, PSP traversed CMEs capturing both remote sensing data and in-situ measurements of the plasma properties and the magnetic field. (Romeo et al. 2023) reported magnetic field variations within a CME containing enhancements, small rotations, and turbulence. Other highlights of the PSP mission are summarized in Raouafi et al. (2023).

Usually 3D reconstructions on the global shape of the CME are performed based on multi-viewpoint images from spacecraft located at 1 AU. From these, the CMEs’ propagation direction, angular width, and tilt are derived (Thernisien et al. 2009; Kouloumvakos et al. 2022). Another method is to obtain the CME direction and speed from elongation measurements of well-observed CME fronts using single spacecraft methods such as Point-P and fixed- $\phi$  methods applied on heliospheric images (see e.g., Kahler & Webb 2007; Wood et al. 2009; Lugaz et al. 2009). However, a recent case study by Patel et al. (2023) yields unrealistic speed results, demonstrating the shortcomings of traditional approaches for deriving kinematics when imaging from close proximity to the transient.

A better approach to derive reliable kinematics and directions of coronal structures or CMEs is the geometric triangulation method developed specifically for WISPR by Liewer et al. (2019, 2020). It leverages the fast motion of the PSP spacecraft and uses the observations of the same event from multiple angles in a short time to perform triangulation with a single spacecraft. This allows us to track and investigate individual small-scale structures, which are part of the global CME. The technique has already been successfully applied in PSP studies to obtain the characteristics of CMEs and other coronal structures (Liewer et al. 2020, 2021, 2022), as well as the deflection (Braga & Vourlidis 2021) and deformation of the CME frontal structures (Braga et al. 2022).

In this study, we investigate the evolution and morphology of small-scale magnetic field structures observed inside a CME, and try to understand their relation to the associated erupted filament imaged by EUV instruments from 1 AU. How do these structures form and develop? How are they related to the larger-scale MFR in which they are embedded? The proximity of WISPR further allows us to study the effect of projection and line-of-sight integration on the CME intensity and to investigate where the small-scale structures are located with respect to the global appearance of the CME.

This paper is organized as follows. In Section 2, we describe the event and observational data used in this study. Section 3 presents the methods used to investigate the small-scale structures observed during the passage of the CME with observations from PSP and also covers the CME 3D global reconstruction. In Section 4 we present our results for the morphology and 3D information, which are discussed and summarized in Section 5. The Appendix A covers a more detailed description of the geometrical triangulation method applied to PSP/WISPR observations.

## 2. Event description and data sources

We investigate the CME event that occurred on December 8, 2022, associated with an eruptive filament over the southwestern limb of the Sun (from Earth view). The first CME front appeared in the LASCO/C2 field of view at 04:12 UT and in C3 at 10:42 UT (at a position angle of  $240^\circ$ ). According to the

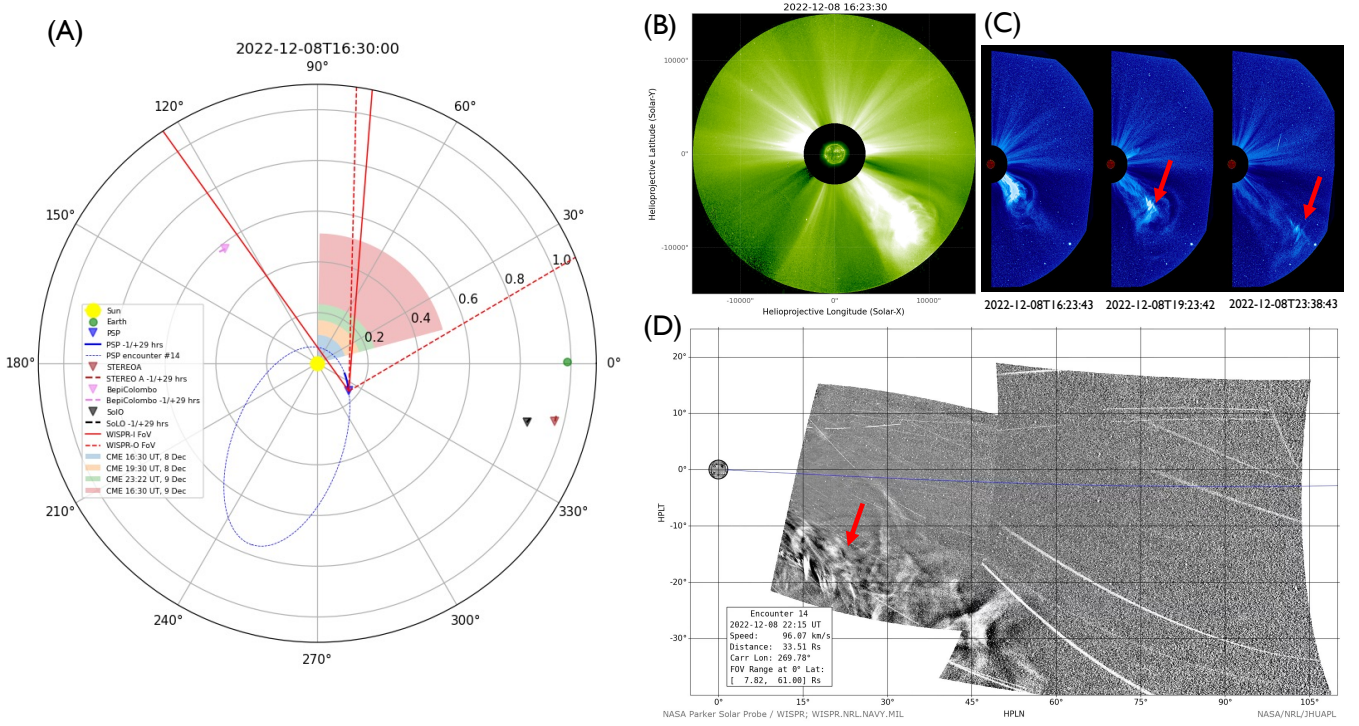


**Fig. 1.** Overview of the December 8, 2022 event showing the spacecraft constellation, using a Heliocentric inertial (HCI) coordinate system, together with white-light imaging data (with EUV inserts from SUVI in 304 Å, and EUVI in 195 Å) recorded from the various spacecraft vantage points (STA/COR2 in panel (B), SOHO/LASCO/C3 in panel (C), and PSP/WISPR in panel (D)). The red arrows in panels (C) and (D) highlight the localized density enhancements, referring to the magnetic fine structures contained in the core of the CME (see Section 4.4). The spacecraft constellation shows PSP orbit for E14 delineated with the blue dashed line, and the PSP trajectory during the event with the blue solid line. PSP longitude changes of  $\sim 24^\circ$  over the entire duration of the event (15:30 UT on December 8 to 23:30 UT on December 9). The FoV of WISPR-I (red solid line) and WISPR-O (red dashed line) are also shown together with the CME propagation direction and width, obtained using the GCS reconstruction results (see Section 4.3), at four different instants of time (16:30 UT [0.11 AU], 19:30 UT [0.17 AU] and 23:22 UT [0.23 AU] on December 8 and 16:30 UT [0.51 AU] on December 9).

SOHO/LASCO CME catalog<sup>1</sup> the CME had a projected linear speed of  $\approx 300$  km/s and an angular width of  $100^\circ$ .

For the event analysis, we used data from various viewpoints and instruments covering the white-light and EUV wavelength ranges. White-light data are obtained from the Solar and Heliospheric Observatory (SoHO; Domingo et al. 1995), located at the Lagrangian point L1, operating two white-light coronagraphs, LASCO/C2 with a field of view (FoV) of  $1.5\text{--}6 R_\odot$  and LASCO/C3 with a FoV of  $3.7\text{--}32 R_\odot$ . The Sun-Earth Connection Coronal and Heliospheric Investigation (SECCHI; Howard et al. 2008) aboard the STEREO-A (STA) spacecraft provides a different perspective. STA observed the event from about 1 AU and  $14^\circ$  West of the Sun-Earth line. We used data from the SECCHI instrument suite including the inner white-light coronagraph COR1 (FoV:  $1.5\text{--}4 R_\odot$ ) and the outer COR2 (FoV:  $2.5\text{--}15 R_\odot$ ) as well as white-light heliospheric imagers, HI-1 and HI-2, covering a FoV up to Earth location and beyond.

Our main focus are the WISPR data, providing unprecedented remote sensing white-light images from a close-in orbit. WISPR comprises two telescopes. The inner one, WISPR-I images an elongation of  $13.5^\circ\text{--}53.0^\circ$ , while the outer, WISPR-O, covers  $50.5^\circ\text{--}108.5^\circ$ . For more details on the WISPR instrument, we refer to Vourlidas et al. (2016).

Due to its highly elliptical orbit, the PSP heliocentric distance and view angle change drastically during its orbit around the Sun. Therefore, the WISPR FoVs and temporal cadences change accordingly. The event under study was observed dur-

ing Encounter 14 (E14). We use observations from December 8, 2022 15 UT to December 9, 2022 23:30 UT. During that time PSP moved from  $-41.9^\circ$  (0.16 AU) to  $-18.2^\circ$  (0.11 AU) in longitude (heliocentric distance) in the Heliocentric Inertial (HCI) coordinate system.

The time cadence increased from  $\sim 30$  min and  $\sim 5$  min as the spacecraft approached the Sun during the event. Furthermore, the event was captured in the 'wave turbulence' mode (WT), where a subfield in WISPR-I is captured at 1 min cadence for several hours. WT data are available from 08:03 UT to 20:53 UT on December 8, 2022. No WISPR-O images are acquired during the WT mode, but WISPR-I full FoV images are available. WT image data allow us to follow the small-scale structures with less ambiguity and to better appreciate the complexity of the CME. We make use of the 'LW'-processed WISPR images for the analysis (see the Appendix in Howard et al. 2022, for more details). The 'LW' technique increases the contrast and facilitates the tracking of the features.

To relate the features observed in white-light to the solar source region, we use available EUV data in the wavelength ranges 171 Å, 195 Å and 304 Å from the Extreme Ultraviolet Imager (EUVI) onboard STA with a FoV up to  $1.7 R_\odot$  (Wuelser et al. 2004). The location of the erupting prominence, being close to the solar limb, allows us to track the event back to the solar surface. For the Earth perspective, we used EUV data from the Solar Ultraviolet Imager (SUVI; Darnel et al. 2022) onboard the Geostationary Operational Environmental Satellite (GOES-R; Krimchansky et al. 2004), which has a FoV similar to EUVI.

<sup>1</sup> [https://cdaw.gsfc.nasa.gov/CME\\_list/](https://cdaw.gsfc.nasa.gov/CME_list/)

We note that we do not discuss the initiation and triggering of the filament eruption itself.

The left panel of Fig. 1 provides an overview of the spacecraft configuration on December 8, 2022 and marks the CME trajectory at different times. The right panels in Fig. 1 show combined COR2/EUVI-195Å (panel B), C3/SUVI-304Å (panel C), and WISPR-I/O composite snapshots (panel D). The COR2 snapshot was obtained at 16:23 UT. The C3 images were taken at 16:23 UT, 19:23 UT, and 23:38 UT and reveal aligned fine structures marked by a red arrow. The WISPR composite, taken at around 22:15 UT (or  $\sim 22.22$  UT in Earth time), shows an incredible amount of detail within the CME, marked with a red arrow as well.

### 3. Methods

Imaging from a single spacecraft cannot directly derive the 3D structure of a CME since it only captures a 2D projection in the plane of the image. Several techniques for CME 3D reconstructions, especially for their extended fronts, were developed during the STEREO era, which offered at least two different vantage points from where CMEs could be observed (see, e.g., Lugaz et al. 2009; Temmer et al. 2009; Byrne et al. 2010; Mierla et al. 2010; Rollett et al. 2016). The most widely used method is the so-called Graduated Cylindrical Shell (GCS) model (Thernisien et al. 2009; Thernisien 2011). The parameters used to define the GCS model are the longitude and latitude at the apex of the CME, its height, the rate of expansion  $\kappa$ , the half-angle  $\alpha$ , which represents the angle between the main axes and half of one leg, and the tilt with respect to the ecliptic plane. We applied GCS on stereoscopic image data from STA and SoHO, both located at about 1 AU (separation angle  $\approx 14^\circ$ ), and PSP. The software package PyThea (Kouloumvakos et al. 2022) was used to perform the GCS reconstruction on the HI-1 data, while the package developed by Von Forstner (2021) was used for the reconstruction on COR2, C3, and WISPR data.

As PSP is moving quite fast (around 160 km/s near the E14 perihelion), the single spacecraft image data can be used to derive the 3D morphology and kinematics. The method is described in Liewer et al. (2020) and details of its application in this study are given in the Appendix A. It assumes that the structures move radially outwards at a constant velocity. Another requirement is that the spacecraft angular position varies sufficiently, for which we take a minimum of  $4^\circ$ . Using Equations A.3 and A.4 we derive the velocity, position, latitude and longitude of a tracked small-scale structure. To solve the equations, we follow the approaches of both Liewer et al. (2020) and Braga & Vourlidas (2021). Uncertainties are estimated by tracking each identified feature at least three times.

## 4. Results

### 4.1. Small-scale structure morphology

In Figures 2–4, we display snapshots of the selected small-scale structures, which we observe as the CME evolves within the FoV of WISPR-I and WISPR-O. All the tracked small-scale structures have been carefully selected considering a significant variation of the HCI longitude of PSP, together with a sufficient visibility/contrast that they need to have over time (see Appendix A). In total we tracked 10 different features over a time of about 32 hours (labeled 0 through 9, in chronological order in which they entered the WISPR-I FoV). In particular, Figure 2 shows the tracked features 0–4 of the CME in a section of the FoV of

WISPR-I, when the instrument is in the WT mode (see Section 2). The tracked features clearly outline curved geometries, which might be related to twisted magnetic field structures. A J-shape structure, that resembles half of a U-shape, is well visible; therefore, we perform a track at its upper edge (feature 0), which stays longer in both FoVs of WISPR-I and WISPR-O with respect to the lower edge. Multiple C-shaped structures are also observed, with track features 1 and 2 located on the “C” upper and lower edges of “C”. Also present is a well-defined thread-like structure (features 3 and 4), typical for filaments.

Figure 3 shows the small-scale structures captured by WISPR-I in synoptic mode. Interesting to note is another C-shape feature, namely feature 5. As the synoptic mode covers a wider FoV, the left panel of Figure 3 reveals the total of features 0–5. Figure 4 shows a later time sequence on 9 December 2022 and the aftermath of the CME. Here a series of blobs (features 6, 7, 8, 9) is visible propagating in the wake of the CME. As time progresses, we notice here how the C-shaped structure at the front expands over time and changes its shape (compare with Figure 2). Because the CME is directed southward, many features tracked in WISPR-I do not reach WISPR-O. In addition, the features become fainter as they move to the outer instrument. As a consequence, only features 0 and 2 can be clearly tracked in the FoV of WISPR-O, as shown in Figure 5. All other features have been tracked using WISPR-I.

### 4.2. Small-scale structure 3D single-spacecraft reconstruction

Over the duration of the event from 15:30 UT on December 8 to 23:30 UT on December 9, PSP longitude varies by about  $\sim 22^\circ$  (HCI; cf. left panel of Figure 1). Each of the ten features was tracked multiple times with at least 3 repetitions and the methods by Braga & Vourlidas (2021) and by (Liewer et al. 2020) were applied to derive their 3D trajectories. Appendix A covers all related plots for deriving the results using the two different approaches. The results are summarized for both methods in Table 1, which gives for each feature the HCI longitude, latitude as well as initial speed and distance. Additionally, we report the angular distance,  $\Delta\phi_1$ , PSP has traveled in longitude (HCI) during the tracking of that specific feature, the angular distance  $\phi_2 - \phi_1$  between the feature and PSP, and finally the morphological group.

Within the uncertainties, we obtain for the tracked features comparable results for all the parameters derived from the two different methods. All the results shown are in HCI coordinate system. In general, all features propagate within a longitudinal range from  $17^\circ$  to  $76^\circ$  and a latitudinal range from  $-23^\circ$  to  $-45^\circ$ . Inspecting the results in Table 1, we find that features 0, 1 and 2 propagate along  $17^\circ$  to  $26^\circ$  in longitude and between  $-23^\circ$  and  $-30^\circ$  in latitude with average speeds of  $\sim 480$  km/s. Feature 5 propagates in a similar direction as features 0–2 (longitude from  $31^\circ$  to  $38^\circ$  and latitude from  $-36^\circ$  to  $-37^\circ$ ), though likely having a lower speed ( $\sim 450$  km/s). Features 3 and 4 propagate along a clearly different direction (longitude between  $69^\circ$  and  $76^\circ$ , latitude from  $-43^\circ$  to  $-45^\circ$ ) with speeds between 300–400 km/s. The blob-like features 6–9 propagate at similar speeds ( $\sim 300$ –400 km/s) and latitudes from  $-31^\circ$  to  $-39^\circ$ , but are distributed over a large longitudinal range between  $24^\circ$  and  $66^\circ$ .

By their similarity in morphology and dynamics, the tracked features can be divided into three groups: group 1 (features: 0, 1, 2, and 5) most likely refers to twisted magnetic field structures with C- and J-shapes, group 2 (features: 3 and 4) to thread-like patterns and group 3 (features: 6, 7, 8, and 9) to blobs propagat-



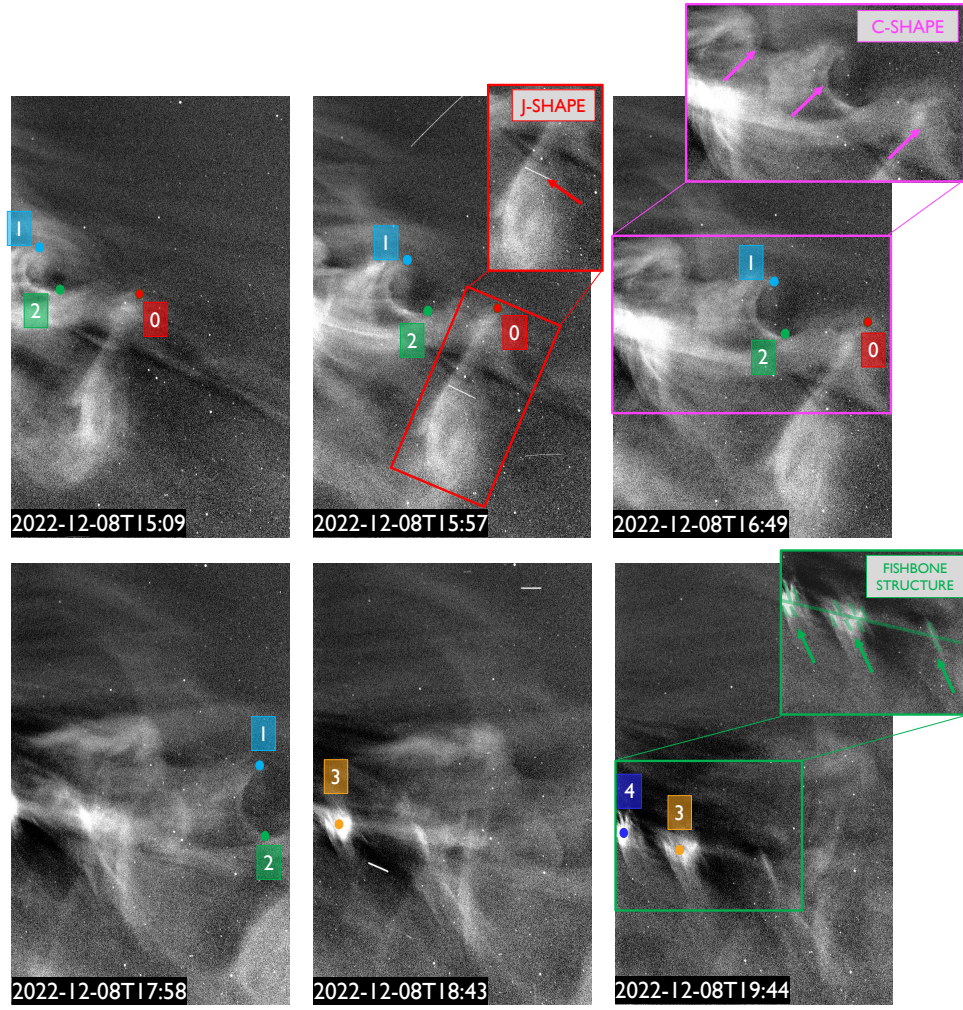


**Fig. 2.** Selected LW-processed snapshots of the WISPR-I WT data set obtained on December 8, 2022 between 15 UT and 20 UT showing the tracked features (labeled 0 through 4). The features tracked belong to structures resembling a J-shape (0) or C-shape (1, 2) as well as being fishbone-like revealing a inclined thread-like pattern (3, 4). The x-axis shows the helioprojective longitude, the y-axis shows the helioprojective latitude. The animation corresponding to this figure is available online in the file movie1.mov.

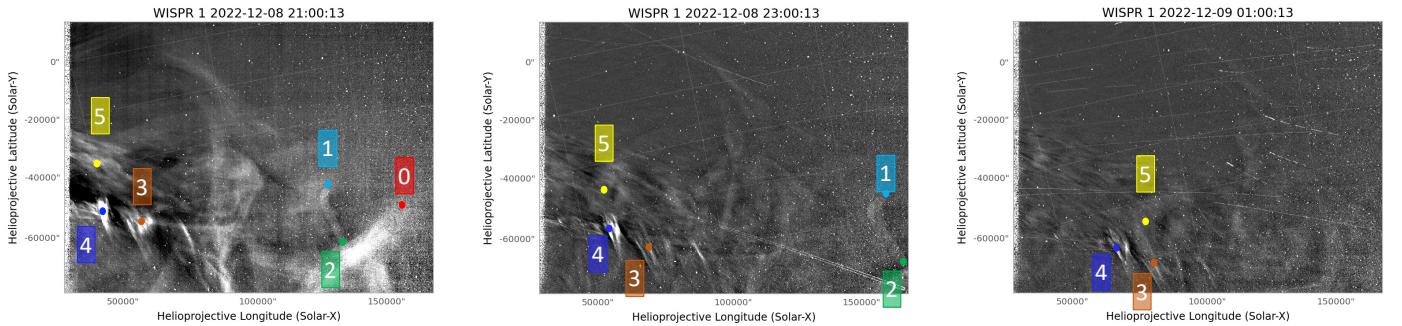


**Fig. 3.** WISPR-I images from December 8 20:30 UT to December 9 18:30 UT and tracked features (0–9). The information from these images are complementary to those from Figure 2.

ing for several hours in the rear part of the CME. On average we see a decreasing trend in speed from the fastest group 1 to the slowest group 3. While each feature of group 1 and 2 shows a clustered behavior, i.e., reveal roughly similar speed, longitude and latitude among each group, the blobs span a wide range of longitudes ( $\sim 40^\circ$ ).

#### 4.3. Global GCS 3D reconstruction

Comparison to the 3D reconstruction of the CME volume allows us to interpret in more detail where the tracked small-scale structures are located with respect to the global appearance of the CME. The free parameters of the GCS model, the apex height of the idealized flux rope, angular width, and aspect ratio, are fitted so as to match the global structure of the CME in stereoscopic images from C3 and COR2. Figure 6 shows the GCS reconstruc-

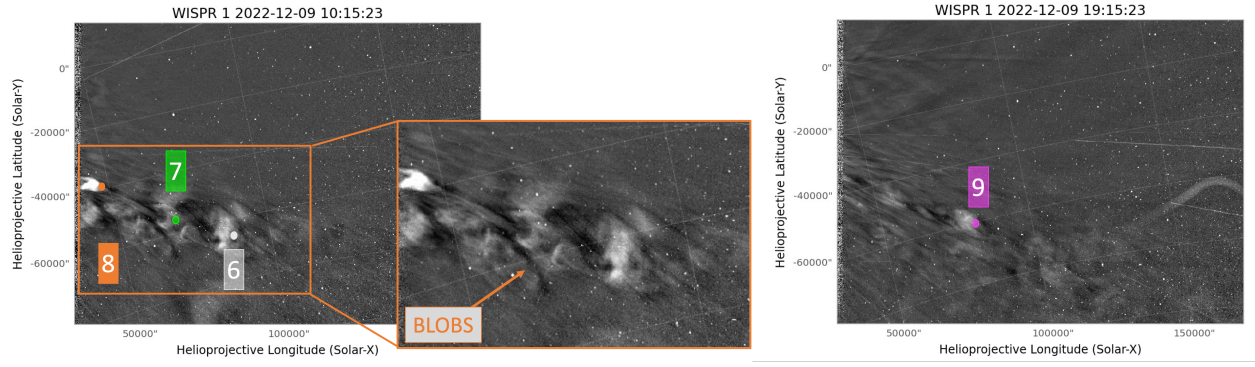


**Fig. 4.** The features 6–9 (blob-like) propagate in the wake of the CME. The information from these images are complementary to those from Figure 2 and 3.

Results of the feature tracking: Braga & Vourlidas (2021) (blue), Liewer et al. (2020) (red)								
ID	$t_0$	$\Delta\phi_1$ (deg)	$\phi_2$ (deg)	$\phi_2 - \phi_1$ (deg)	$\delta_2$ (deg)	$v_0$ (km/s)	$r_0$ ( $R_\odot$ )	group
0	2022-12-08T15:00:45.635	6.2	$22 \pm 3$ $19 \pm 4$	$64$ $61$	$-25 \pm 1$ $-26 \pm 2$	$500 \pm 40$ $464 \pm 62$	$12.0 \pm 1.0$ $11.0 \pm 1.0$	1
1	2022-12-08T15:00:45.635	4.3	$26 \pm 2$ $32 \pm 9$	$66$ $74$	$-23 \pm 1$ $-25 \pm 3$	$460 \pm 50$ $492 \pm 106$	$10.0 \pm 1.0$ $10.0 \pm 2.0$	1
2	2022-12-08T15:00:45.635	7.4	$26 \pm 8$ $17 \pm 8$	$67$ $59$	$-30 \pm 3$ $-29 \pm 3$	$486 \pm 80$ $395 \pm 54$	$11 \pm 1.0$ $11 \pm 1.0$	1
3	2022-12-08T18:30:45.637	5.0	$71 \pm 11$ $69 \pm 10$	$111$ $109$	$-43 \pm 2$ $-43 \pm 1$	$383 \pm 100$ $386 \pm 50$	$14.0 \pm 1.0$ $13.0 \pm 0.4$	2
4	2022-12-08T19:30:45.638	6.3	$76 \pm 5$ $70 \pm 10$	$116$ $110$	$-45 \pm 1$ $-45 \pm 1$	$350 \pm 50$ $293 \pm 57$	$13.0 \pm 1$ $13.0 \pm 0.2$	2
5	2022-12-08T21:30:48.797	7.2	$31 \pm 2$ $38 \pm 8$	$70$ $77$	$-36 \pm 1$ $-37 \pm 2$	$426 \pm 50$ $467 \pm 47$	$9.0 \pm 0.2$ $9.0 \pm 0.6$	1
6	2022-12-09T04:38:21.002	3.9	$58 \pm 4$ $53 \pm 5$	$92$ $86$	$-39 \pm 1$ $-39 \pm 1$	$316 \pm 25$ $296 \pm 20$	$9.0 \pm 1.0$ $8.0 \pm 0.1$	3
7	2022-12-09T07:00:41.103	5.4	$43 \pm 2$ $45 \pm 6$	$76$ $78$	$-35 \pm 1$ $-35 \pm 4$	$400 \pm 10$ $391 \pm 20$	$9 \pm 0.1$ $9.0 \pm 0.1$	3
8	2022-12-09T10:00:41.107	5.4	$24 \pm 6$ $38 \pm 6$	$55$ $69$	$-31 \pm 2$ $-35 \pm 1$	$300 \pm 50$ $351 \pm 20$	$9 \pm 1.0$ $8.0 \pm 0.2$	3
9	2022-12-09T16:30:48.811	7.1	$64 \pm 8$ $66 \pm 4$	$89$ $91$	$-37 \pm 1$ $-38 \pm 1$	$416 \pm 50$ $425 \pm 22$	$8.0 \pm 1.0$ $8.0 \pm 0.4$	3

**Table 1.** Results in HCI obtained by applying the methods discussed in Section 3 to the features labeled in Figures 2 and 3. ID is the label of the feature,  $t_0$  is the initial time at which each feature is tracked,  $\Delta\phi_1$  is the variation in the longitude of the PSP spacecraft during the tracking of the specific feature,  $\phi_2$  and  $\delta_2$  is the derived longitude and latitude, respectively, while  $v_0$  and  $r_0$  are the initial velocity and position of the feature. The last column represents the group in which the different features belong, see Section 4.2. In blue we show the results obtained with the fitting method of Braga & Vourlidas (2021), while in red the one of Liewer et al. (2020) (see Appendix A for more details).

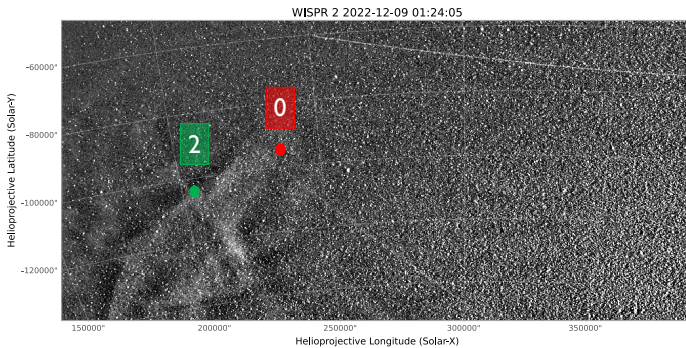


**Fig. 5.** WISPR-O images on December 8 23:39 UT and December 9 01:39 UT with tracked features 0 and 2.

tion at  $\sim 16:30$  UT on December 8, 2022. The GCS fit indicates a propagation direction for the apex roughly along  $52^\circ$  in longitude and  $-42^\circ$  in latitude (HCI coordinates) with uncertainties in the range of about  $10^\circ$  for latitude and longitude, respectively (for detailed estimates on the accuracy of the GCS method we refer to Verbeke et al. 2023). The GCS geometry is described by the results  $\alpha=22^\circ$ ,  $\kappa=0.26$  rad and a tilt of  $-52^\circ$ . From this we calculate the angular width face-on ( $\omega_{FO}$ ), which describes the lateral extension of the CME, by  $\omega_{FO}=2(\alpha+\delta)$  with  $\delta=\sin^{-1}\kappa$ , together with the edge-on angular width  $\omega_{EO}=2\delta$  (see Table 1 in Thernisien 2011). According to this, the CME has a half-width  $\omega_{FO}$  of  $\sim 37^\circ$  and an angular width at the edge  $\omega_{EO}$  of  $\sim 30^\circ$ . Therefore, the CME is spanning from about 15 to 89 in HCI longitude and from  $-12$  to  $-72$  in latitude.



Next, we expand the GCS fit to the inner Heliosphere combining HI-1 and WISPR-I data<sup>2</sup>. For that we used the GCS results derived from stereoscopic image data combining C3 and COR2 at  $\sim 16:30$  UT, kept all other parameters constant, and simply changed the height over time to match the CME front as observed in the heliospheric image data pairs. Figure 7 shows the GCS model applied to images from HI-1 and WISPR-I, at  $\sim 17:00$  UT ( $H = 24 R_{\odot}$ ),  $\sim 19:30$  UT ( $H = 36 R_{\odot}$ ), and  $\sim 23:22$  UT ( $H = 50 R_{\odot}$ ). With this we derive a 3D CME speed of about 650 km/s. We observed distinct differences in the appearance of the CME between WISPR and HI-1. The WISPR images contain more small-scale structures, but the broad outer envelope is missing. The latter is clearly visible in both COR2 and HI-1.

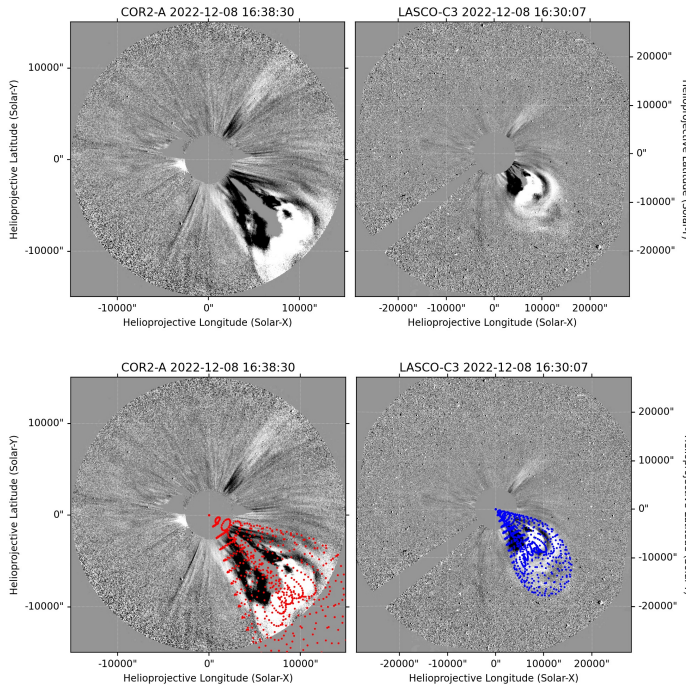


**Fig. 6.** GCS reconstruction on the running difference coronagraph images of COR2 and C3 at  $\sim 16:30$  UT.

To visualize the location of the different features in 3D and relate the results in Table 1 with those of GCS, we calculate the position of each small-scale structure at 16:30 UT on December 9, 2022 ( $t_0$  of feature 9). Using the derived 3D speed, we extrapolate the height of the GCS apex accordingly to  $110 R_{\odot}$  for the same time. Figure 8 shows the resulting 3D distribution of the features with respect to the central axis of the GCS located at  $\Delta\phi = 0$  deg,  $\Delta\delta = 0$  deg and spanning  $0$ – $110 R_{\odot}$  in height. The tracked small-scale structures are shown in boxes whose color depends on the morphological group discussed in Section 4.2. Features 0–7 are all found to lie within the GCS reconstructed volume and can therefore be safely interpreted as being CME internal small-scale structures. Comparing the location of the different groups, as listed in Table 1, to the central axis of the GCS, we find that features 0, 1, 2 and 5 are located in

the eastern leg of the CME, while features 3 and 4 are part of the western leg.

The blobs, covering tracked features 6–7, seem to be located at the rear part of the CME and close to the inner regions of each flank. We note that features 8 and 9 appear to lie outside of the legs modeled by GCS by about  $10^\circ$ , which is in the range of uncertainties of the GCS parameters (Verbeke et al. 2023). We note that we did not include the tilt in the visualization.

#### 4.4. Relation to the erupting filament

To better understand the white-light morphology of the CME and its small-scale structures, we correlated the CME with the solar surface structures and their dynamics, as observed in EUV. This event can be clearly associated with a filament eruption from the southwestern limb of the Sun. Figure 9 shows a polar projection view of the composite SUVI images in the  $304\text{\AA}$  and the  $171\text{\AA}$  filters. We note that the filament begins crossing the western solar limb on December 4, and we can follow its height over the surface. The eruption and first appearance of the CME in COR1 occurs on December 8, 2022 at  $\sim 1$  UT. In the lower corona ( $< 5 R_{\odot}$ ) the filament rises at a speed of  $11 \pm 4$  km/s, reaching about  $310 \pm 18$  km/s (kinematics are not shown) after the eruption ( $> 9 R_{\odot}$ ). As the filament lifts off, a hot (green,  $195\text{\AA}$ ) 'horn'-shaped structure (Figure 9, white arrow) offers evidence of a MFR, followed by cool (red,  $304\text{\AA}$ ) radial structures highly reminiscent of filament fine structures.

In Figure 10, we show combined EUVI and coronagraph images where we can clearly follow the evolution of these features from EUV to the white-light images. Specifically, panels (A)–(D) show composite EUVI  $171/304\text{\AA}$  images with COR1 data on December 8 between 01:23 and 11:39 UT. The white arrow indicates the hot 'horn' shape, while the red arrow points to the cool filament material. In panels (E) and (F) we show COR2 images one hour apart from each other. We mark on those images the WISPR tracked features that can be identified in the COR2 images. Combining EUV and coronagraph data, we associate features 0, 1 and 2 with the typical shapes that we find in filaments during their evolution. Features 3 and 4 instead appear to be related to the core of the CME, indicated by the red arrow in the COR1 images (panels (A)–(D)). In Figure 1 panel (C), we also mark with red arrows thread patterns observed in C3 that might be related to features 3 and 4 as observed in WISPR images (panel (D) from Figure 1, or in more detail shown in Figure 2).

## 5. Discussion and conclusions

The internal structure of CMEs has been explored in the past but the new generation of white-light instruments, such as WISPR, deliver images with much higher sensitivity thanks to the unprecedented orbit of PSP. These images hold interesting results, not fully explored yet, about characteristics of the MFR evolving into interplanetary space.

We study the CME event on December 8, 2022 that is related to an eruptive filament. The eruption occurred close to the western limb of the Sun and is observed in white-light by multiple spacecraft located at different distances and vantage points. While the STA and SoHO spacecraft, close to 1 AU and separated by  $14^\circ$ , remain almost constant in their position, PSP is close to the Sun and changes in distance from 0.16 AU to 0.11 AU and in longitude by  $\sim 24^\circ$  during the CME observing time of 32 hours. Using the fast motion of PSP, we investigate

<sup>2</sup> We note that a  $\sim 7$  minute time delay between observations from 1 AU (STA) and from 0.11–0.16 AU (PSP) should be considered to account for the light travel time difference between PSP and the spacecraft at 1 AU.



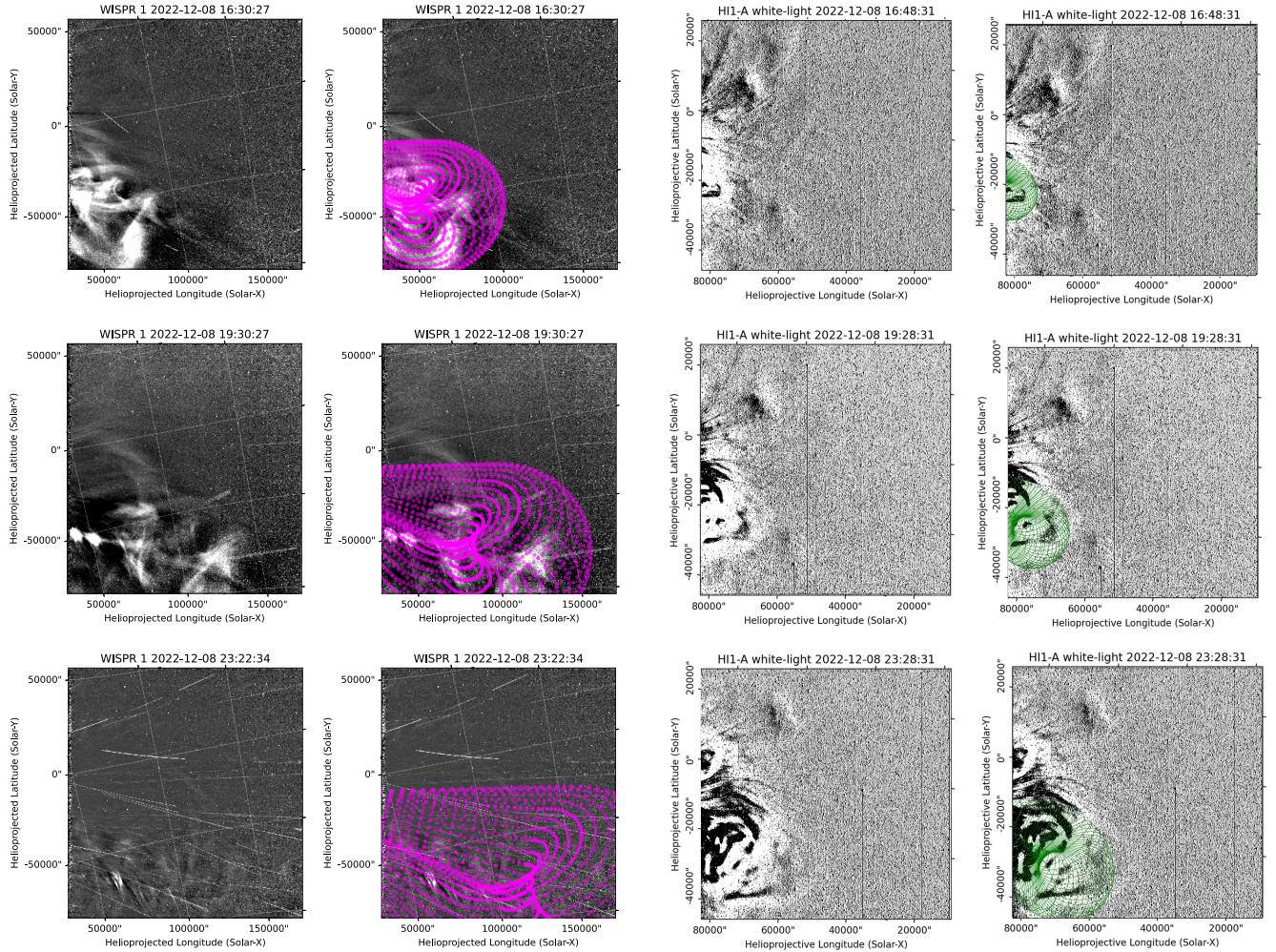


**Fig. 7.** GCS reconstruction on the heliospheric images of HI-1 and WISPR 1 at three instant of time.

WISPR data using a 3D reconstruction method as described in Section 3 and Appendix A. We track 10 well-observed small-scale density structures in WISPR images (Figures 2, 3 and 4). The results enable us to categorize the tracked features and to locate them in the context of the global CME appearance derived from GCS reconstruction.

Based on their morphology, propagation direction, and dynamics we find three different groups of features. Group 1 covers a C- or J-shaped appearance (features 0, 1, 2, 5), group 2 are density patterns characterized by aligned threads (features 3, 4), and group 3 covers blobs (features 6, 7, 8, 9). C- and J-shapes features can be interpreted as plasma-containing twisted magnetic field structures, commonly observed in CMEs. Concave-upward features are frequently observed in EUV, e.g., in our study by SUVI and EUVI (see the ‘horns’ pointed with white arrows in Figures 9 and 10), and may be indicators of the extent of the flux rope cavity (Vourlidis et al. 2013). The EUV horns have an appearance similar to the C- and J-shapes observed in WISPR, which suggests coronal temperatures for these features. The high-density blobs observed are usually related to plasmoid instabilities in the post-CME current sheet (see, e.g., Ciaravella & Raymond 2008; Schanche et al. 2016; Di Matteo et al. 2019; Poirier et al. 2023; Webb & Vourlidis 2016; Lee et al. 2020). We find numerous blobs propagating in the rear part of the CME under study in a time window of approximately 22 hours. The

blobs are derived to move slower by about 100 km/s with respect to the features tracked at the front of the CME.

The thread-like features (group 2) appear localized on a global fishbone structure with a certain angle to that backbone. As these trace the magnetic field fine structure, they might refer to some sheared field with confined density enhancement. They likely resemble cool plasma material as observed in EUV at chromospheric temperatures (see red arrow in Figure 9 and 10), evolving into localized structures during the filament eruption. This can be compared to other prominence eruption studies. For example Su et al. (2015) reports a series of vertical threads aligned along an elongated structure, together with associated U-shape and blob features likely to be related to signatures of magnetic reconnection. In general, we notice that the high-resolution data from WISPR allow to relate in more detail CME small-scale structures to typical elements of a filament (see e.g., Parenti 2014). This might shed more light on the early evolution of the internal structure of CMEs and contributes to a better understanding of why such a low number of CMEs covering prominence material is detected in-situ (see e.g., Niembro et al. 2023).

Relating the tracked magnetic structures to the global CME structure, we find interesting results. To reconstruct the CME flux rope structure in 3D we used the GCS model (see Figure 8). We obtain that all features of group 1 are clearly located within the CME’s eastern part of the CME. Group 2 is also found to

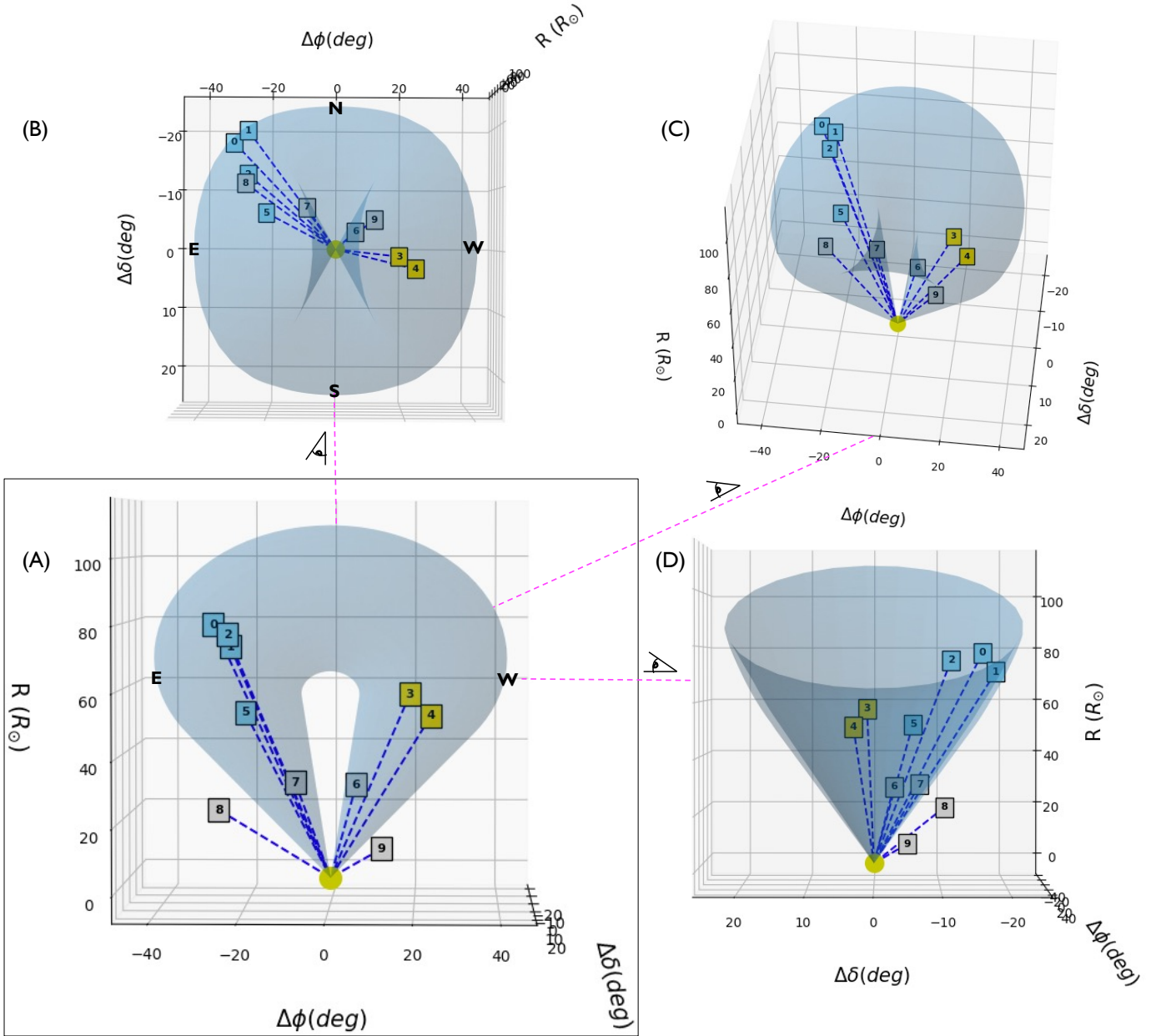


**Fig. 8.** Comparison of the positions of the local magnetic structures, summarized in Table 1, together with the global CME flux rope modeled by GCS. All panels show 3D plots in a  $\Delta\phi$ ,  $\Delta\delta$ ,  $R$  plane at 16:30 UT on December 9, 2022.  $\Delta\phi$  and  $\Delta\delta$  are the relative variation in longitude and latitude with respect to the central axis of the GCS, while  $R$  is the height. W indicates the west, E the east, S the south and N the north. The eye represents the point of view of the observer. The colors of the boxes indicate the different families to which the features 0-9 belong: 1 (azure), 2 (yellow) and 3 (gray). The plot shows: (A) the frontal view of the GCS modeled flux-rope and the relative location of the features with respect to its central axis, (B) shows the extension of the flux rope from a top view, (C) shows it from a west-top view, (D) shows it from the western leg. An animation of this image is available in the online material of this article.

be clearly located in the western leg of the CME. In comparison to that, the blobs from group 3 are distributed over a large longitudinal range of  $\sim 40^\circ$  and do not show a clustered behavior. With respect to the derived GCS geometry, all blobs (features 6–9) are located at the edges of the CME eastern and western flanks, respectively. Features 8 and 9 even outside of the reconstructed flux rope. This may hint toward either the spatial extent of the post-CME current sheet, hence its three-dimensionality, or to the possible influence of the ambient corona in the evolutionary behavior of the CS (e.g., Bemporad et al. 2006; Lin et al. 2015) leading eventually to a secondary source for the formation of the blobs. A clear distinction between these two processes is not possible due to the uncertainties related to both, the PSP

reconstruction and GCS method (see Section 3). But we encourage further studies on relating small-scale density structures to the global CME appearance for better constraining their physical generation processes.

The combined views from SoHO, STA, and PSP allow us to compare the 3D shape of the global CME appearance from 1 AU and from 0.11–0.16 AU. Interestingly, we found that WISPR does not detect the outer CME envelope, in contrast to the HI-1 images that clearly show the typical bubble-like front (see Figure 7). Because PSP is much closer to the CME than SoHO and STA, WISPR line-of-sight through the CME is much shorter than for the 1 AU imagers. Therefore, the broad outer front is being ‘resolved out’ in WISPR images. On the other hand, due



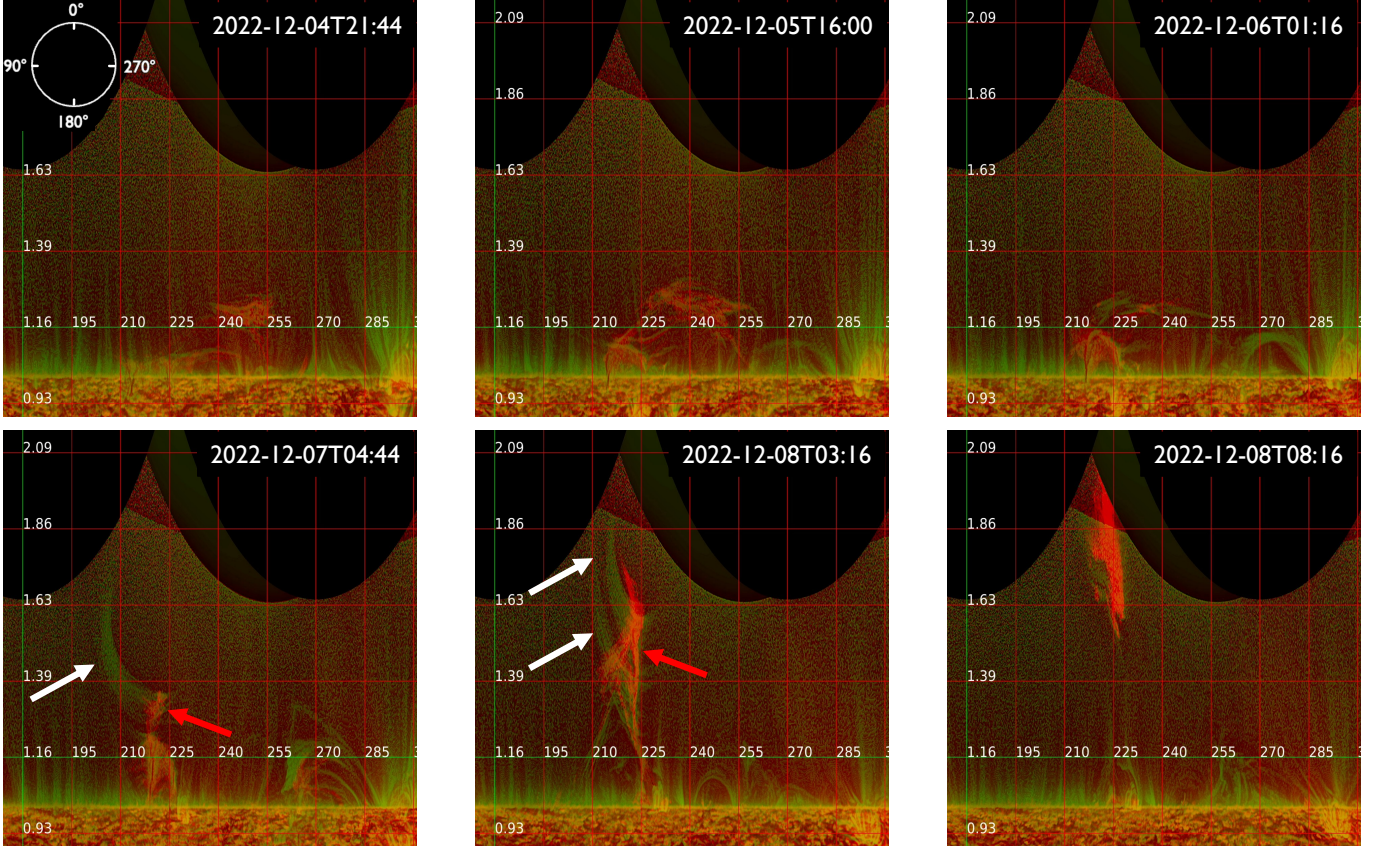


**Fig. 9.** Polar view of the solar prominence and its eruption in composite images of  $304\text{\AA}$  and  $171\text{\AA}$  observed by SUVI from December 4 to December 8. In the y-axis the height in solar radii, while in the x-axis the position angle is given. For orientation, in the top left corner a sketch of the PA is given, where  $0^\circ$  corresponds to the Solar North. The image is produced by JHelioviewer (Müller et al. 2017). The animation corresponding to this figure is available online in the file movie2.mov.

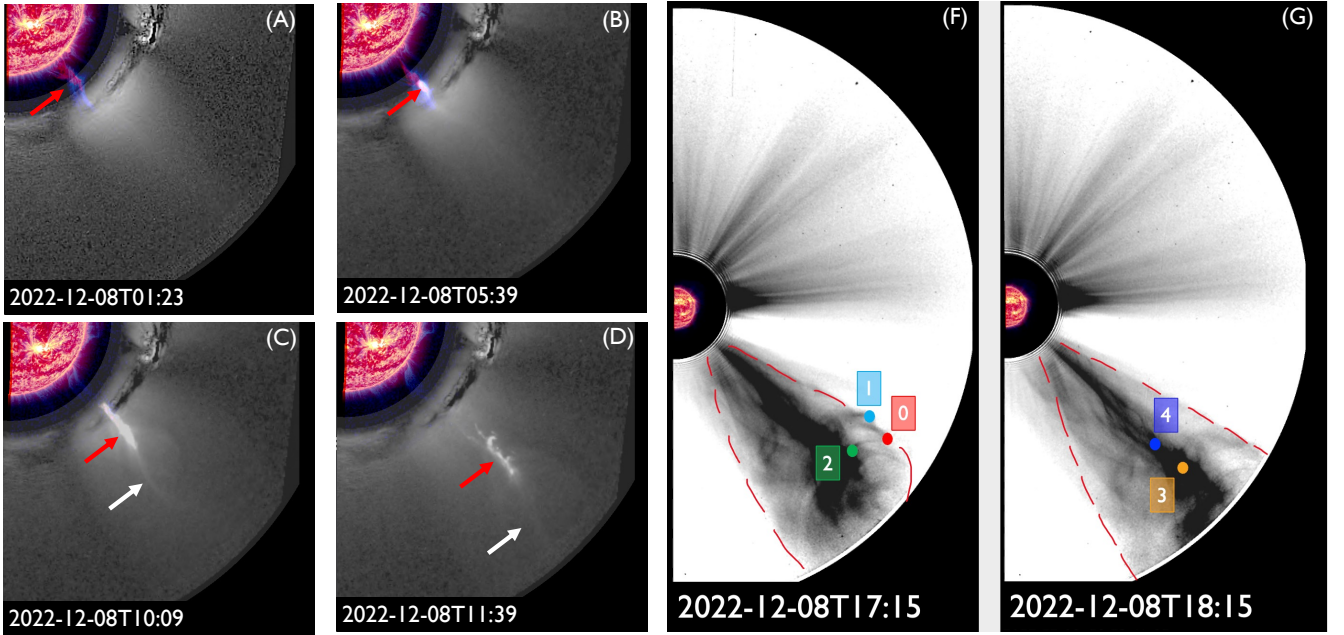


**Fig. 10.** Evolution of the CME between the EUV instruments and coronagraphs. Panels (A)-(D) show composite EUVI 171 (blue)/ $304\text{\AA}$  (red) images and STA/COR1 on December 8 between 01:23 and 11:39 UT. The white arrow indicates the hot 'horn'-shape and the red arrow points to the cool filament material. Panels (F) and (G) show the features tracked in WISPR images with COR2 identifications (see Figure 2).

to its closer proximity, WISPR gives higher signals for small-scale structures in the CME body (see also e.g., Vourlidas et al. 2016; Nisticò et al. 2019; Hess et al. 2020, 2021). We also notice that similar effects, namely a different appearance of coronal EUV waves at the solar surface as viewed from different vantage points, were explained by the integration of intensity along different lines-of-sight (e.g., Patsourakos & Vourlidas 2009).

We conclude that CME flux ropes might consist of different magnetic fine structures that evolve differently. These results are relevant for future CME propagation and forecasting models, especially those that implement magnetized flux ropes (e.g., Török et al. 2018; Verbeke et al. 2019). To accurately interpret the observed density structures of a CME, which trace magnetic structures, it is therefore essential to gather image data from various distances. This approach offers complementary perspectives on the CME's appearance, accounting for projection and line-of-sight integrated density effects that influence its visual presentation.

## Appendix A: Single-spacecraft reconstruction fits

As described in Section 3, PSP can be used as a single-spacecraft to obtain the kinematic and position of features belonging to the observed CME. The CME small-scale structures we investigate are faint to be revealed and tracked through the WISPR-I and WISPR-O FoVs, therefore we use so-called “LW-processed” images (described in detail in Appendix A in Howard et al. 2022). This approach exploits the time domain at each pixel location to obtain a smooth background (at the 5th-percentile level) in a time interval centered at the time of each image.

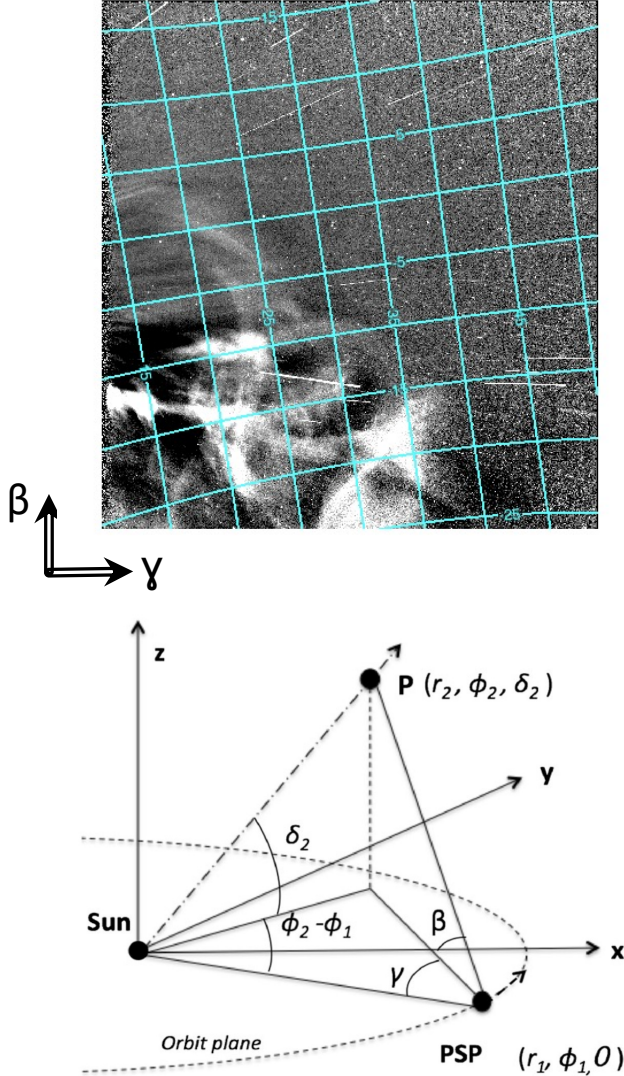


**Fig. A.1.** On the top, an example of the grid used by the IDL routine `wispr_camera_coords` to measure the projected angles in WISPR images, respectively the angle out of the plane  $\beta$  and the elongation  $\gamma$ . On the bottom, a schematic of the geometry used taken from (Liewer et al. 2019), where PSP’s orbit is approximated to be in the solar equatorial plane, and through which we derive the geometrical equations (Equations A.3 and A.4).

Figure A.1 describes the geometry for reconstructing trajectories of small-scale structures in the WISPR FoV. We are in-

terested in their location with respect to the Sun at a specific time  $t$ , that is given by  $r_2(t)$ . In addition, we want to obtain for each feature its longitude  $\phi_2$  and its latitude  $\delta_2$  in a heliocentric solar equatorial coordinate system, such as the heliocentric inertial reference frame (HCI). Approximating PSP’s orbit to be in the solar equatorial plane, PSP’s coordinates are given by  $[r_{\text{PSP}}, \phi_{\text{PSP}}, \delta_{\text{PSP}}] = [r_1, \phi_1, 0]$ . PSP observes a point-like feature in the WISPR FoV that is identified by two projected angles, the elongation  $\gamma$  in PSP’s orbital plane and the angle out of this plane  $\beta$ , as illustrated in Figure A.1. These angles are obtained by tracking the feature over time and converting its coordinate from pixel to PSP orbital frame coordinates using the SolarSoft/IDL routine `wispr_camera_coords`, accounting for effects of spacecraft location, projection and distortion of the instruments (see more details in Braga & Vourlidas 2021). Each of the identified features was tracked at least three times, to ensure the track of the same feature over time. This allows to estimate the uncertainties in the results obtained according to the approach followed by Braga & Vourlidas (2021). From these different tracks, Liewer et al. (2020) obtains the average  $\beta$  and  $\gamma$  at each time, and also estimates the uncertainties in the  $\beta$  and  $\gamma$  measurements, and uses these uncertainties to estimate the errors in the parameters of the reconstructed trajectory of a feature.

From the measured  $\gamma(t)$  and  $\beta(t)$  of a specific feature, we determine the unknowns  $r_2$  (defined as  $r_2(t) = r_0 + v_0 * t$ , with  $v_0$  and  $r_0$  its constant speed and position at the initial time  $t_0$ ),  $\phi_2$ , and  $\delta_2$  by fitting the following two geometrical equations:

$$\beta(t) = \text{atan}\left(\frac{\tan \delta_2 \sin(\gamma(t))}{\sin[\phi_2 - \phi_1(t)]}\right), \quad (\text{A.1})$$

$$\cot(\gamma(t)) = \frac{r_1(t) - r_2(t) \cos \delta_2 \cos([\phi_2 - \phi_1(t)])}{r_2(t) \cos \delta_2 \sin([\phi_2 - \phi_1(t)])}, \quad (\text{A.2})$$

These two equations provide the conversion between the observed positions ( $\beta$  and  $\gamma$ ) of a feature with respect to WISPR and the feature’s 3D position in the heliocentric inertia reference frame, assuming that PSP’s orbit is in the solar equatorial plane. Note that PSP’s orbit is inclined to the solar equator by a small angle  $\epsilon \approx 4^\circ$ . The above equations are therefore modified to include the correction due to the inclination  $\epsilon$ .

$$\beta(t) = \text{atan}\left(\frac{\tan \delta_2 \sin(\gamma(t))}{\sin[\phi_2 - \phi_1(t)]} (1 - F \sin \epsilon)\right), \quad (\text{A.3})$$

$$\cot(\gamma(t)) = \frac{r_1(t) - r_2(t) \cos \delta_2 \cos([\phi_2 - \phi_1(t)])}{r_2(t) \cos \delta_2 \sin([\phi_2 - \phi_1(t)])} (1 - G \sin \delta_2 \sin \epsilon), \quad (\text{A.4})$$

where  $G$  and  $F$  specify the first order corrections, and their expressions are given in the Appendix of Liewer et al. (2020). With PSP’s position ( $\phi_1$ ,  $r_1$  and  $\epsilon$ ) known, and assuming a radial motion at a constant speed, a feature’s trajectory ( $\phi_2$ ,  $\delta_2$ ,  $r_0$  and  $v_0$ ) can be determined from a sequence of  $\gamma(t)$  and  $\beta(t)$  measurements.

So far, two different approaches have been adopted by the scientific community to solve these equations in order to obtain its unknowns. Liewer et al. (2020) solves the equations containing the  $\epsilon$  term, A.3 and A.4, performing a Levenberg–Marquardt least-squares fit (see Appendix B of Liewer et al. 2020, for a discussion on deriving initial guess parameters). Instead, Braga & Vourlidas (2021) solves the simplified equations, and finds the



best  $\phi_2(t)$  and  $\delta_2(t)$  by substituting simultaneously in Equations A.1 and A.2 the initial guess for each unknown that is set to vary within a certain range that is decided from the user a priori. Then the results are converted to the system of reference of the spacecraft in order to consider the inclination of PSP to the Solar equatorial plane. Once the equations are solved per each set of initial guess, the best fit is computed using the residuals. Indeed, the solution is the one that allows to derive the  $\beta_{der}$  and  $\gamma_{der}$ , through Equations A.1 and A.2, which have the smallest deviation with respect to the measured ones,  $\beta_{mes}$  and  $\gamma_{mes}$ . In this study, we use both approaches.

Figures A.2 and A.3 show the related calculation steps and plots to the solving schemes for Equations A.3 and A.4 using the two different approaches by Liewer et al. (2020) and Braga & Vourlidas (2021), respectively, for all tracked features (0–9). The features were carefully selected considering a significant variation of the longitude of PSP during its observation to satisfy the condition for applying the reconstruction methods (Section 3).

Figure A.2 shows for each feature the plots of the evolution of the elongation  $\gamma$  and  $\beta$  over time. The measured angles and their 1- $\sigma$  uncertainties, calculated considering the three different tracked performed per each substructure, are shown in black. In red we shown the computed  $\gamma$  and  $\beta$  using the best-fitting parameters derived by forward-fitting Equations A.3 and A.4. The  $\beta$  angle can be also computed with a different equation (see Liewer et al. 2020), which is shown in blue.

Figure A.3 shows per each feature to the left the best value of the unknown parameters obtained with the residuals technique. We notice how per each feature the best parameter chosen to perform the fit on the measurement is the one where the minimum of the residual function is located. The right panels show instead the plots of the evolution of the elongation  $\gamma$  and  $\beta$  over time. The red crosses indicate the measurements performed of the angles, while the solid black line shows the fit.

In this study, the trajectories of the tracked features are determined with two approaches, and in both cases, we assume that a feature moves radially with a constant speed; namely,  $\phi_2$ ,  $\delta_2$ ,  $v_0$  are all constant. A relatively large deviation of the computed  $\gamma$  and  $\beta$  from the measurements, as shown in a few panels in Figure A.2 may indicate that the motion of some of these features is not exactly radial at times. We will discuss these deviations in future work. The experiments on deriving time-dependent longitude and latitude are described by (Braga & Vourlidas 2021).

**Acknowledgements.** G.M.C. and M.T. acknowledge support from the Young Researchers Program (YRP), project number AVO165300016. A.V. and G.S. are supported by WISPR Phase-E funds. C.R.B. acknowledges the support from the NASA STEREO/SECCHI (NNG17PP27I) program and NASA HGI grant 80NSSC23K0412. The work of P.C.L. was conducted at the Jet Propulsion Laboratory, California Institute of Technology under a contract from NASA. J. Q. is supported by NASA HGI grant 80NSSC22K0519. A.K. acknowledges financial support from NASA HTM grant 80NSSC24K0071. V.B. acknowledges funding of the CGAUSS project as German contribution to the WISPR camera on Parker Solar Probe by the German Space Agency through the German Bundesministerium für Wirtschaft und Klimaschutz under FKZ: 50OL2301. G.M.C. thanks Iulia Ana Maria Chifu for fruitful discussions on the WISPR field of view, as well as Paulo Penteado for the support on the SolarSoft/WISPR IDL package. Parker Solar Probe was designed, built, and is now operated by the Johns Hopkins Applied Physics Laboratory as part of NASA's Living with a Star (LWS) program (contract NNN06AA01C). Support from the LWS management and technical team has played a critical role in the success of the Parker Solar Probe mission. The Wide-Field Imager for Parker Solar Probe (WISPR) instrument was designed, built, and is now operated by the US Naval Research Laboratory in collaboration with Johns Hopkins University/Applied Physics Laboratory, California Institute of Technology/Jet Propulsion Laboratory, University of Gottingen, Germany, Centre Spatial de Liege, Belgium and University of Toulouse/Research Institute in Astrophysics and Planetology. The SECCHI data are produced by an international consortium of the NRL, LMSAL, and NASA GSFC (USA), RAL and U. Bham (UK), MPS (Germany), CSL (Bel-

gium), IOTA, and IAS (France). The SOHO/LASCO data used here are produced by a consortium of the Naval Research Laboratory (USA), Max-Planck-Institut fuer Aeronomie (Germany), Laboratoire d'Astronomie (France), and the University of Birmingham (UK). SOHO is a project of international cooperation between ESA and NASA. SUVI was designed and built at Lockheed-Martin's Advanced Technology Center in Palo Alto, California.

Software: JHelioviewer <sup>3</sup>, has been used as a visualisation tool for solar data from different instruments (Müller et al. 2017). This research has made use of PyThea v0.7.4, an open-source and free Python package to reconstruct the 3D structure of CMEs and shock waves (Zenodo: <https://doi.org/10.5281/zenodo.5713659>). We also used GCS in Python v0.2.2 (Zenodo: <https://zenodo.org/badge/latestdoi/297350666>), which is a python 3 implementation of the Graduated Cylindrical Shell model based on the existing IDL implementation in SolarSoft. Other python(v3.9) libraries used for this work are: astropy (Astropy Collaboration et al. (2018)), matplotlib (Hunter (2007)), numpy (van der Walt et al. (2011)), pandas (Reback et al. (2020)), scipy (Virtanen et al. (2020)), SunPy (SunPy Community et al. (2020)). The SolarSoft <sup>4</sup> package in IDL(v8.6.0) has been used in this paper. Also the WISPR package on Solarsoft has been widely used.

<sup>3</sup> <https://www.jhelioviewer.org/>

<sup>4</sup> <https://soho.nascom.nasa.gov/solarsoft/>

## References

- Amari, T., Luciani, J. F., Aly, J. J., Mikic, Z., & Linker, J. 2003, *ApJ*, 595, 1231
- Astropy Collaboration, Price-Whelan, A. M., Sipőcz, B. M., et al. 2018, *AJ*, 156, 123
- Aulanier, G. & Schmieder, B. 2002, *A&A*, 386, 1106
- Bemporad, A., Poletto, G., Suess, S. T., et al. 2006, *ApJ*, 638, 1110
- Bohlin, J. D., Frost, K. J., Burr, P. T., Guha, A. K., & Withbroe, G. L. 1980, *Sol. Phys.*, 65, 5
- Braga, C. R. & Vourlidas, A. 2021, *A&A*, 650, A31
- Braga, C. R., Vourlidas, A., Liewer, P. C., et al. 2022, *ApJ*, 938, 13
- Brueckner, G. E., Howard, R. A., Koomen, M. J., et al. 1995, *Sol. Phys.*, 162, 357
- Byrne, J. P., Maloney, S. A., McAteer, R. T. J., Refojo, J. M., & Gallagher, P. T. 2010, *Nature Communications*, 1, 74
- Chen, P. F. 2011, *Living Reviews in Solar Physics*, 8, 1
- Chen, P. F., Harra, L. K., & Fang, C. 2014, *ApJ*, 784, 50
- Ciaravella, A. & Raymond, J. C. 2008, *The Astrophysical Journal*, 686, 1372
- Darnel, J. M., Seaton, D. B., Bethge, C., et al. 2022, *Space Weather*, 20, e2022SW003044, e2022SW003044 2022SW003044
- DeVore, C. R. & Antiochos, S. K. 2000, *ApJ*, 539, 954
- Di Matteo, S., Viall, N. M., Kepko, L., et al. 2019, *Journal of Geophysical Research (Space Physics)*, 124, 837
- Domingo, V., Fleck, B., & Poland, A. I. 1995, *Sol. Phys.*, 162, 1
- Forbes, T. G. 2000, *J. Geophys. Res.*, 105, 23153
- Fox, N. J., Velli, M. C., Bale, S. D., et al. 2016, *Space Sci. Rev.*, 204, 7
- Gopalswamy, N. 2022, *Atmosphere*, 13, 1781
- Green, L. M., Török, T., Vršnak, B., Manchester, W., & Veronig, A. 2018, *Space Sci. Rev.*, 214, 46
- Guo, J. H., Zhou, Y. H., Guo, Y., et al. 2021, *ApJ*, 920, 131
- Hess, P., Howard, R. A., Stenborg, G., et al. 2021, *Sol. Phys.*, 296, 94
- Hess, P., Rouillard, A. P., Kouloumvakos, A., et al. 2020, *ApJS*, 246, 25
- Howard, R. A., Moses, J. D., Vourlidas, A., et al. 2008, *Space Sci. Rev.*, 136, 67
- Howard, R. A., Stenborg, G., Vourlidas, A., et al. 2022, *ApJ*, 936, 43
- Howard, R. A., Vourlidas, A., & Stenborg, G. 2023, *Frontiers in Astronomy and Space Sciences*, 10
- Hunter, J. D. 2007, *Computing in Science and Engineering*, 9, 90
- Illing, R. M. E. & Hundhausen, A. J. 1983, *J. Geophys. Res.*, 88, 10210
- Kahler, S. W. & Webb, D. F. 2007, *Journal of Geophysical Research (Space Physics)*, 112, A09103
- Kaiser, M. L., Kucera, T. A., Davila, J. M., et al. 2008, *Space Science Review*, 136, 5
- Kouloumvakos, A., Rodríguez-García, L., Gieseler, J., et al. 2022, *Frontiers in Astronomy and Space Sciences*, 9, 974137
- Krimchansky, A., Machi, D., Cauffman, S., & Davis, M. 2004, *Proceedings of SPIE - The International Society for Optical Engineering*, 5570
- Lee, J.-O., Cho, K.-S., Lee, K.-S., et al. 2020, *ApJ*, 892, 129
- Liewer, P., Vourlidas, A., Thernisien, A., et al. 2019, *Sol. Phys.*, 294, 93
- Liewer, P. C., Qiu, J., Ark, F., et al. 2022, *Sol. Phys.*, 297, 128
- Liewer, P. C., Qiu, J., Penteado, P., et al. 2020, *Sol. Phys.*, 295, 140
- Liewer, P. C., Qiu, J., Vourlidas, A., Hall, J. R., & Penteado, P. 2021, *A&A*, 650, A32
- Lin, J., Murphy, N. A., Shen, C., et al. 2015, *Space Sci. Rev.*, 194, 237
- Lugaz, N., Vourlidas, A., & Roussev, I. I. 2009, *Annales Geophysicae*, 27, 3479
- Mierla, M., Inhester, B., Antunes, A., et al. 2010, *Annales Geophysicae*, 28, 203
- Mishra, W. & Teriaca, L. 2023, *Journal of Astrophysics and Astronomy*, 44, 20
- Moore, R. L., Sterling, A. C., Hudson, H. S., & Lemen, J. R. 2001, *ApJ*, 552, 833
- Müller, D., Nicula, B., Felix, S., et al. 2017, *A&A*, 606, A10
- Niembro, T., Seaton, D. B., Hess, P., et al. 2023, *Frontiers in Astronomy and Space Sciences*, 10, 1191294
- Nisticò, G., Bothmer, V., Liewer, P., Vourlidas, A., & Thernisien, A. 2019, *Nuovo Cimento C Geophysics Space Physics C*, 42, 21
- Okamoto, T. J., Tsuneta, S., Berger, T. E., et al. 2007, *Science*, 318, 1577
- Parenti, S. 2014, *Living Reviews in Solar Physics*, 11, 1
- Patel, R., West, M. J., Seaton, D. B., et al. 2023, *ApJ*, 955, L1
- Patsourakos, S. & Vourlidas, A. 2009, *Astrophysical Journal*, 700, L182–L186
- Poirier, N., Réville, V., Rouillard, A. P., Kouloumvakos, A., & Valette, E. 2023, *A&A*, 677, A108
- Pulkkinen, T. 2007, *Living Reviews in Solar Physics*, 4, 1
- Raouafi, N. E., Matteini, L., Squire, J., et al. 2023, *Space Sci. Rev.*, 219, 8
- Reback, J., McKinney, W., Jbrockmendel, et al. 2020, *pandas-dev/pandas: Pandas 1.0.5*
- Riley, P., Lionello, R., Mikić, Z., et al. 2007, *ApJ*, 655, 591
- Rollett, T., Möstl, C., Isavnin, A., et al. 2016, *ApJ*, 824, 131
- Romeo, O. M., Braga, C. R., Badman, S. T., et al. 2023, *ApJ*, 954, 168
- Ruan, G., Schmieder, B., Mein, P., et al. 2018, *ApJ*, 865, 123
- Schanche, N. E., Reeves, K. K., & Webb, D. F. 2016, *ApJ*, 831, 47
- Schmieder, B., Démoulin, P., & Aulanier, G. 2013, *Advances in Space Research*, 51, 1967
- Schmieder, B., Tian, H., Kucera, T., et al. 2014, *A&A*, 569, A85
- Su, Y., van Ballegoijen, A., McCauley, P., et al. 2015, *ApJ*, 807, 144
- SunPy Community, Barnes, W. T., Bobra, M. G., et al. 2020, *ApJ*, 890, 68
- Tandberg-Hanssen, E. 1995, *The nature of solar prominences*, Vol. 199
- Temmer, M. 2021, *Living Reviews in Solar Physics*, 18, 4
- Temmer, M. & Bothmer, V. 2022, *A&A*, 665, A70
- Temmer, M., Preiss, S., & Veronig, A. M. 2009, *Sol. Phys.*, 256, 183
- Temmer, M., Scolini, C., Richardson, I. G., et al. 2023, *arXiv e-prints*, arXiv:2308.04851
- Thernisien, A. 2011, *ApJS*, 194, 33
- Thernisien, A., Vourlidas, A., & Howard, R. A. 2009, *Sol. Phys.*, 256, 111
- Török, T., Downs, C., Linker, J. A., et al. 2018, *ApJ*, 856, 75
- van der Walt, S., Colbert, S. C., & Varoquaux, G. 2011, *Computing in Science and Engineering*, 13, 22
- Verbeke, C., Mays, M. L., Kay, C., et al. 2023, *Advances in Space Research*, 72, 5243
- Verbeke, C., Pomoell, J., & Poedts, S. 2019, *A&A*, 627, A111
- Virtanen, P., Gommers, R., Oliphant, T. E., et al. 2020, *Nature Methods*, 17, 261
- Von Forstner, J. L. F. 2021, *johan12345/gcs\_python: Release 0.2.2*
- Vourlidas, A., Howard, R. A., Plunkett, S. P., et al. 2016, *Space Sci. Rev.*, 204, 83
- Vourlidas, A., Lynch, B. J., Howard, R. A., & Li, Y. 2013, *Sol. Phys.*, 284, 179
- Vršnak, B. 2001, *Sol. Phys.*, 202, 173
- Webb, D. F., Burkepile, J., Forbes, T. G., & Riley, P. 2003, *Journal of Geophysical Research (Space Physics)*, 108, 1440
- Webb, D. F. & Cliver, E. W. 1995, *J. Geophys. Res.*, 100, 5853
- Webb, D. F. & Vourlidas, A. 2016, *Sol. Phys.*, 291, 3725
- Wood, B. E., Howard, R. A., Plunkett, S. P., & Socker, D. G. 2009, *ApJ*, 694, 707
- Wuelser, J.-P., Lemen, J. R., Tarbell, T. D., et al. 2004, in *Society of Photo-Optical Instrumentation Engineers (SPIE) Conference Series*, Vol. 5171, *Telescopes and Instrumentation for Solar Astrophysics*, ed. S. Fineschi & M. A. Gummin, 111–122
- Zhang, J., Temmer, M., Gopalswamy, N., et al. 2021, *Progress in Earth and Planetary Science*, 8, 56



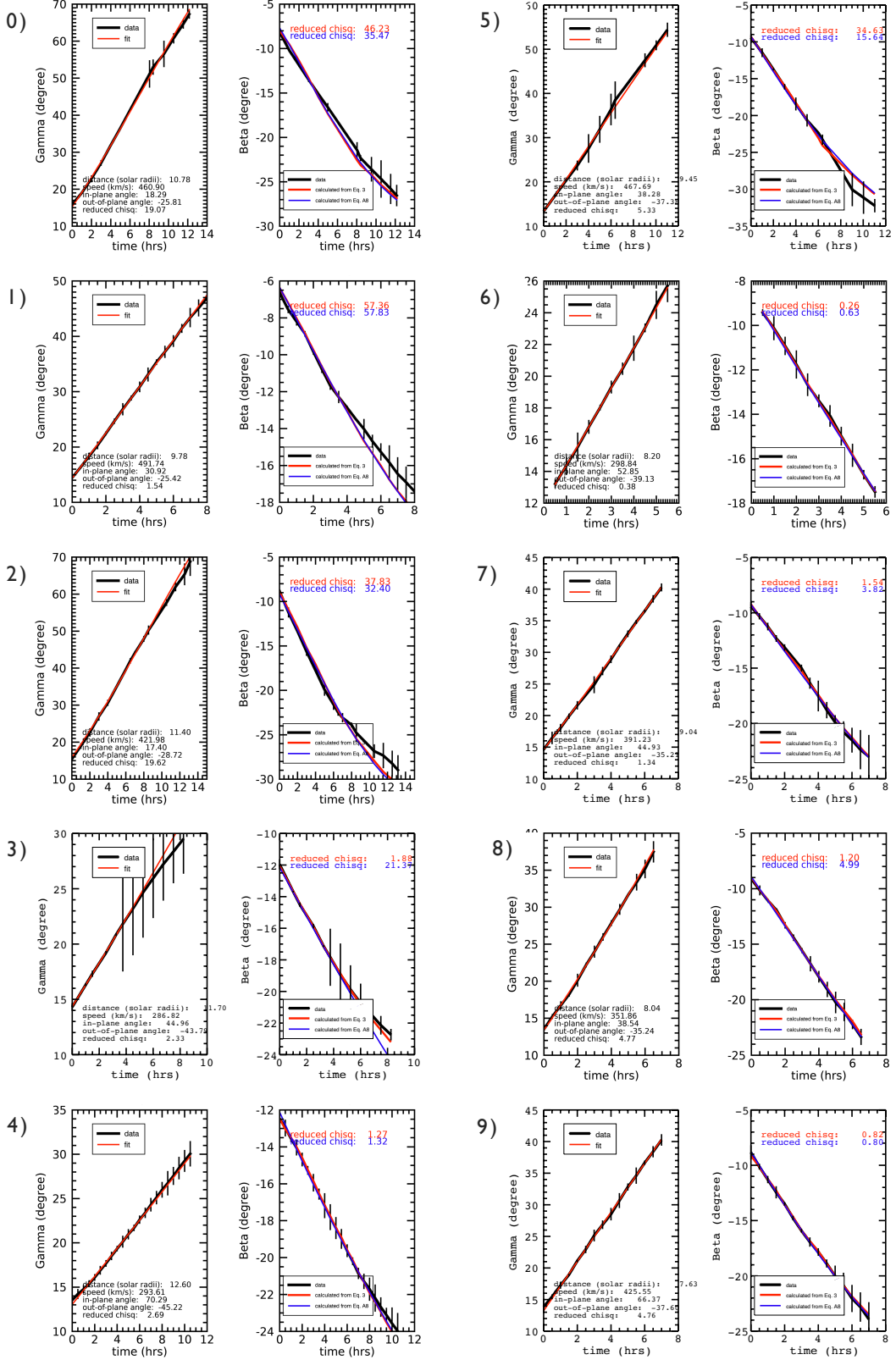


**Fig. A.2.** Results obtained for features (0 to 9) using the approach of (Liewer et al. 2020).

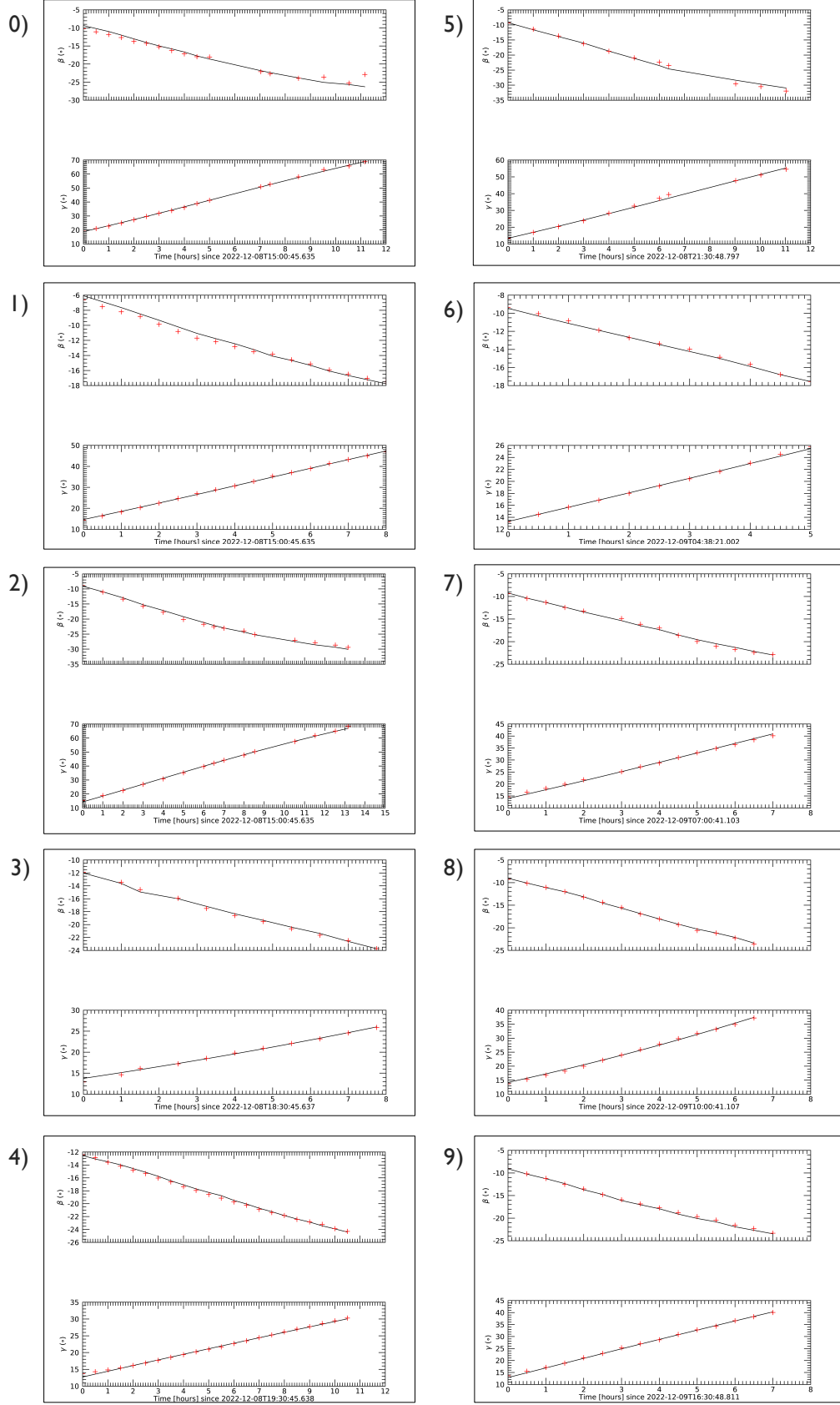


**Fig. A.3.** Results obtained for features (0 to 9) using the approach of (Braga & Vourlidas 2021). The red crosses are the measured angles  $\alpha$  and  $\beta$ , while the solid black line indicated the fit on the equations discussed in the Appendix A with the parameters shown in Table 1.